Electronic Supplementary Information (ESI)

The Promise of Operational Stability in Pnictogen-Based Perovskite-Inspired Solar Cells

Noora Lamminen,[a] Joshua Karlsson,[a] Ramesh Kumar,[b] Noolu Srinivasa Manikanta Viswanath,[c] Snigdha Lal,[d] Francesca Fasulo,[e] Marcello Righetto,[d] Mokurala Krishnaiah,[a] Kimmo Lahtonen,[f] Amit Tewari,[g] Atanas Katerski,[h] Jussi Lahtinen,[a] Ilona Oja Acik,[h] Erik M. J. Johansson,[b] Ana Belén Muñoz-García,[e] Michele Pavone,[i] Laura M. Herz,[d] G. Krishnamurthy Grandhi,*[a] Paola Vivo*[a]

[a] Hybrid Solar Cells, Faculty of Engineering and Natural Sciences, Tampere University, P.O. Box 541, Tampere, FI-33014 Finland

[b] Department of Chemistry, Ångström Laboratory, Uppsala University, Box 523, SE 75120 Uppsala, Sweden

[c] Division of Materials Science and Engineering, Hanyang University 222 Wangsimni-ro, Seongdong-gu, Seoul 04763, Republic of Korea

[d] Clarendon Laboratory, Department of Physics, University of Oxford, Parks Road, Oxford, OX1 3PU, United Kingdom

[e] Department of Physics "Ettore Pancini" University of Naples Federico II Comp. Univ. Monte Sant'Angelo Naples 80126, Italy

[f] Faculty of Engineering and Natural Sciences Tampere University P.O. Box 692, Tampere FI-33014, Finland

[g] Faculty of Information Technology and Communication Sciences, Tampere University, 33720 Tampere, Finland

[h] Department of Materials and Environmental Technology, Tallinn University of Technology, Ehitajate tee 5, Tallinn, Estonia

[i] Department of Chemical Sciences University of Naples Federico II Comp. Univ. Monte Sant'Angelo Naples 80126, Italy

*Emails: murthy.grandhi@tuni.fi, paola.vivo@tuni.fi

Contents

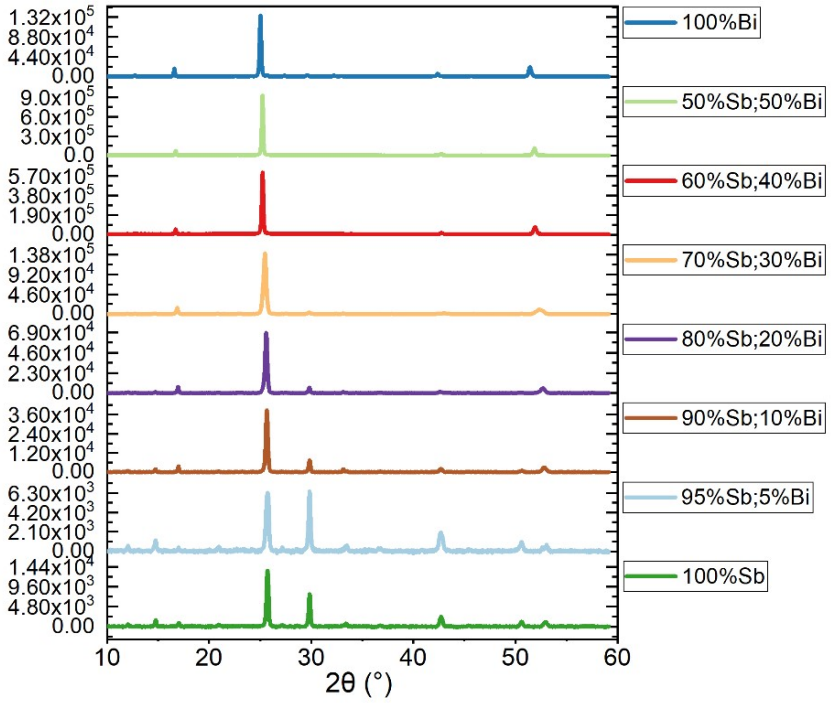

Figure S1. The XRD patterns of CsMAFA-Sb:Bi films with varying loading Sb-Bi ratios, processed in DMF.

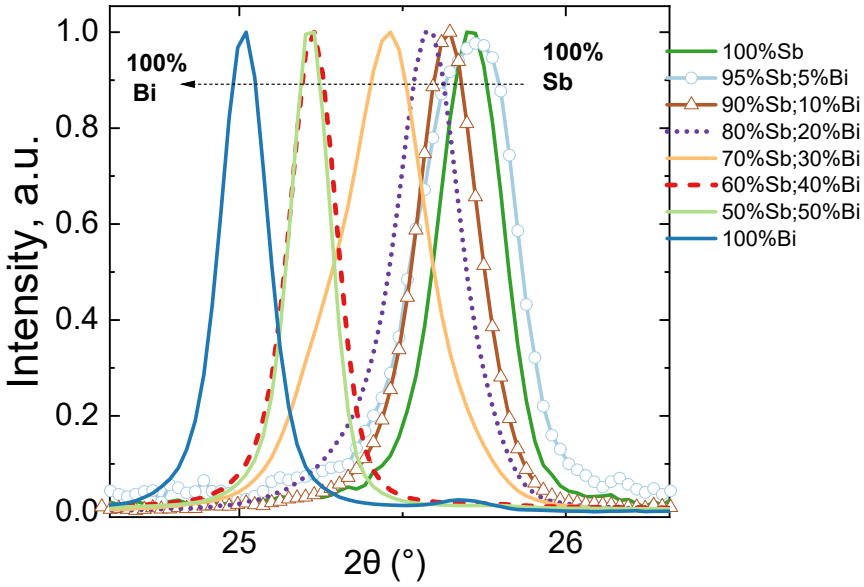

Figure S2. The normalized XRD patterns of the mixed Sb-Bi ratio films main characteristic peak.

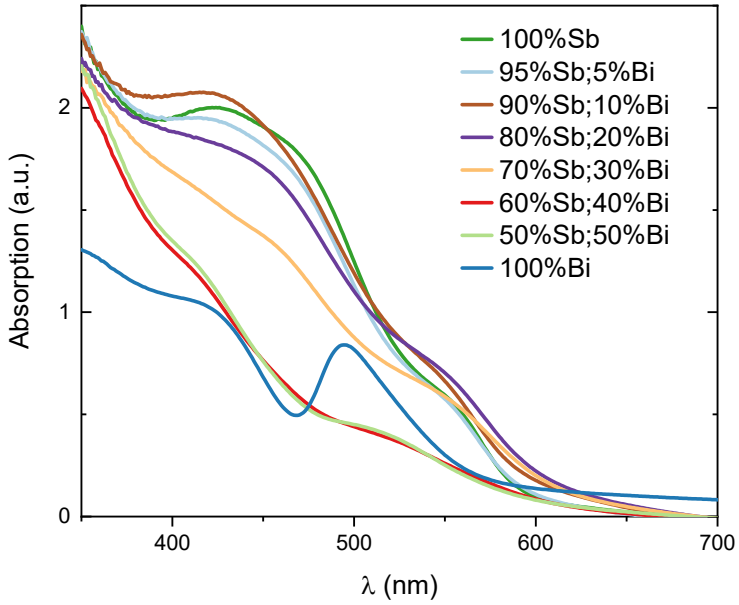

Figure S3. The absorbance spectra of the CsMAFA-Sb:Bi films with varying Sb and Bi content.

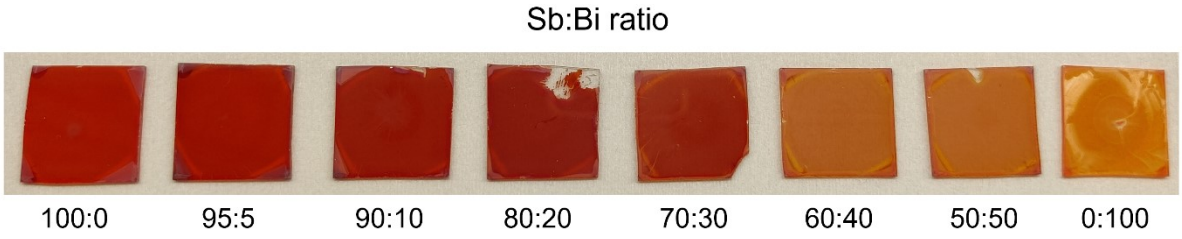

Figure S4. Photographs (under room light) of CsMAFA-Sb:Bi films with varying loading Sb:Bi ratios, processed in DMF.

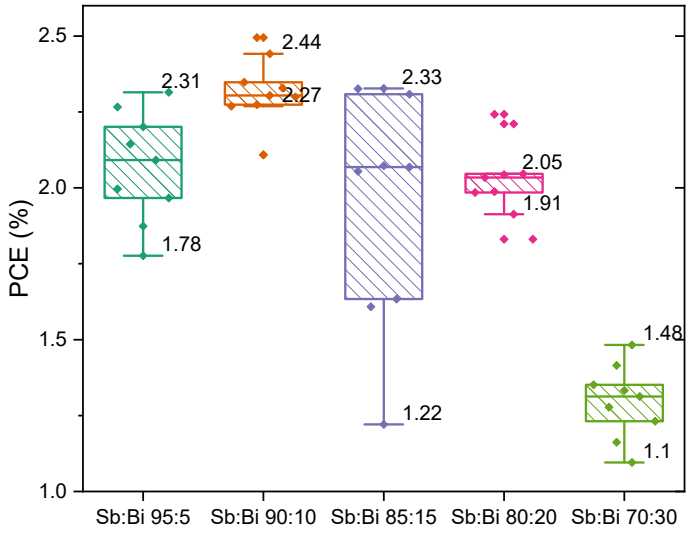

Figure S5. PCE variation of devices as a function of stoichiometric Sb:Bi molar ratio.

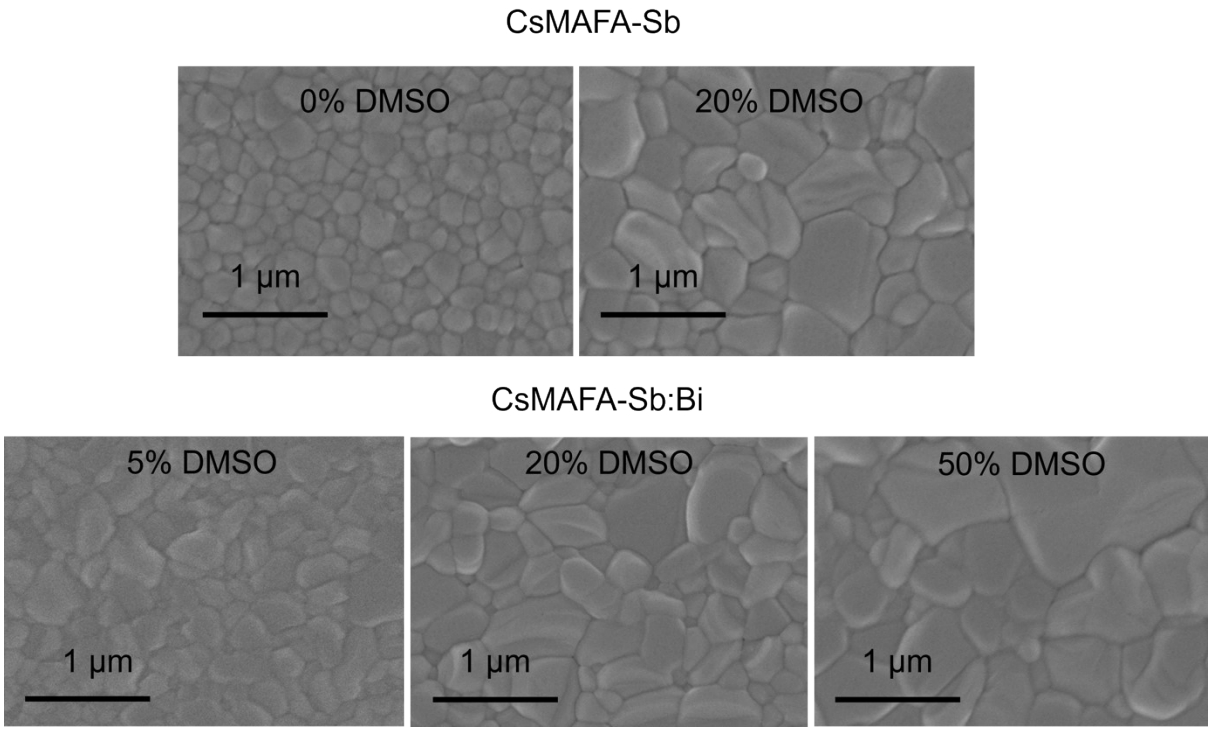

Figure S6. SEM images of CsMAFA-Sb and CsMAFA-Sb:Bi films made from precursors with different amounts of DMSO.

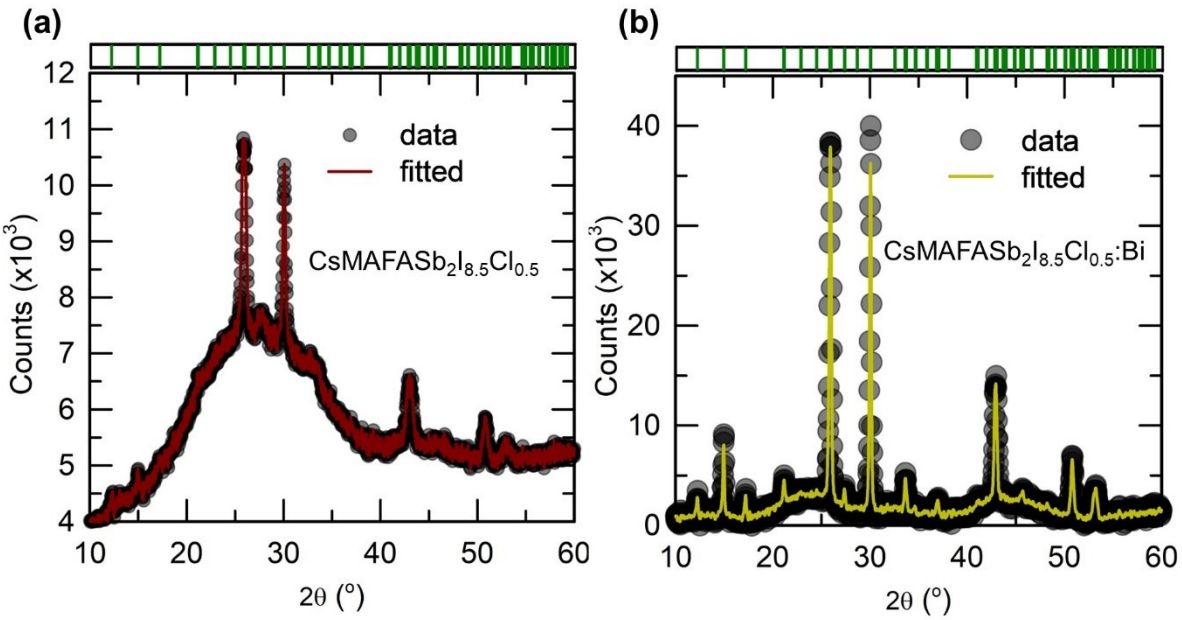

Figure S7. Experimental XRD patterns and the corresponding Rietveld refinement fits of (a) CsMAFA-Sb and (b) CsMAFA-Sb:Bi films.

Supplementary note 1

In CsMAFA-Sb:Bi, the structure deviates from the typical 3D interconnected framework of conventional perovskites. Instead of forming a continuous network, $[Sb/Bi]I_6$ octahedra pair up to create $(Sb/Bi)_2(I/Cl)_9$ dimers, each consisting of two edge-sharing $[Sb/Bi]I_6$ units. These dimers do not form a 3D network but are either isolated or arranged into layers, depending on the variant. However, in this crystal structure, the dimers are entirely isolated, leading to a quasi-0D structure where each $(Sb/Bi)_2(I/Cl)_9$ unit functions as an independent "molecular" entity (**Figure 1**). This reduction in dimensionality—from 3D to 2D or quasi-0D—enhances the material's stability by preventing the long-range structural degradation seen in 3D perovskites, particularly under environmental stress. The isolated or layered nature of the $(Sb/Bi)_2(I/Cl)_9$ units, along with the larger A-site cations, helps stabilize the structure, making CsMAFA-Sb:Bi more durable and suitable for long-term applications.

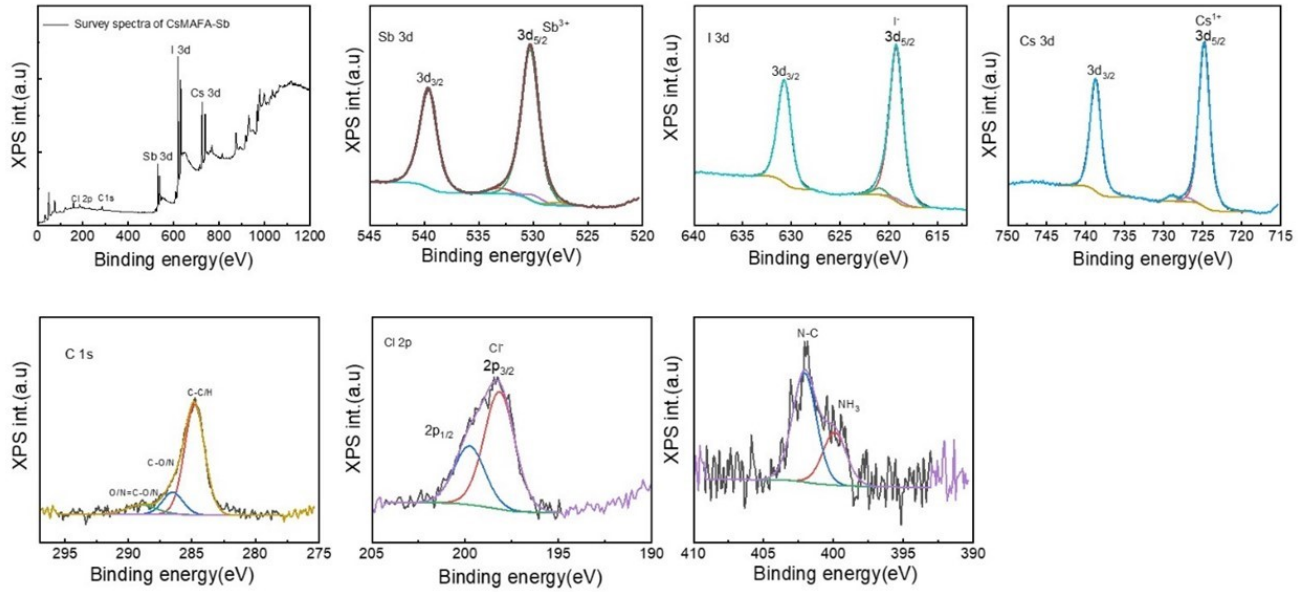

Figure S8. XPS survey spectra and core levels of Cs 3d, Sb 3d, I 3d, C 1s, Cl 2p, and N 1s of CsMAFA-Sb.

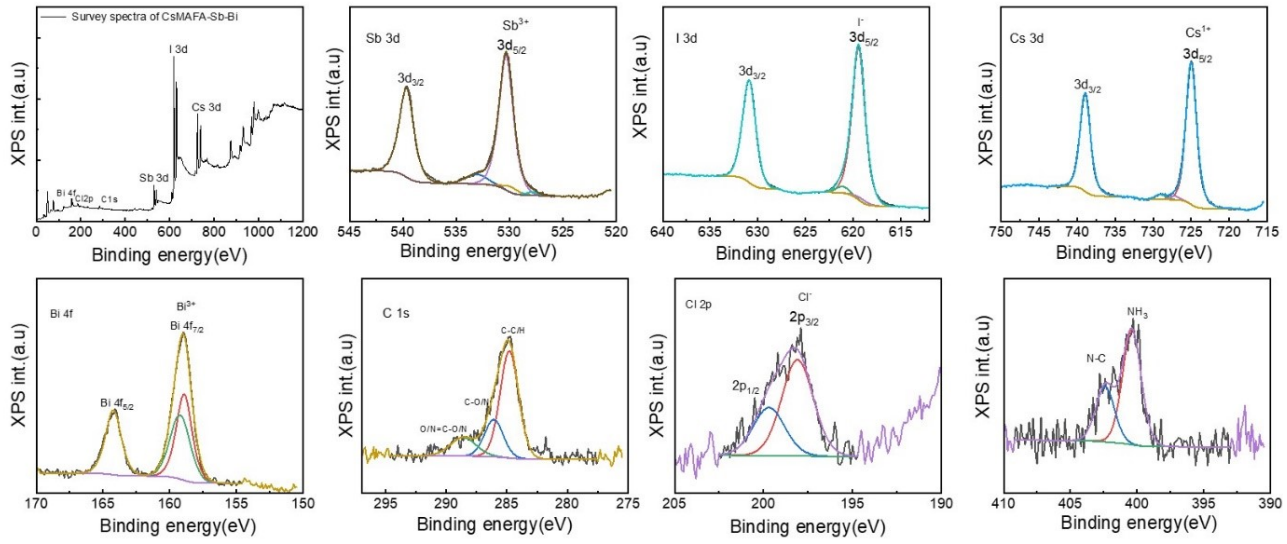

Figure S9. XPS survey spectra and core levels of Cs 3d, Sb 3d, Bi 4f, I 3d, C 1s, Cl 2p, and N 1s for a CsMAFA-Sb:Bi film.

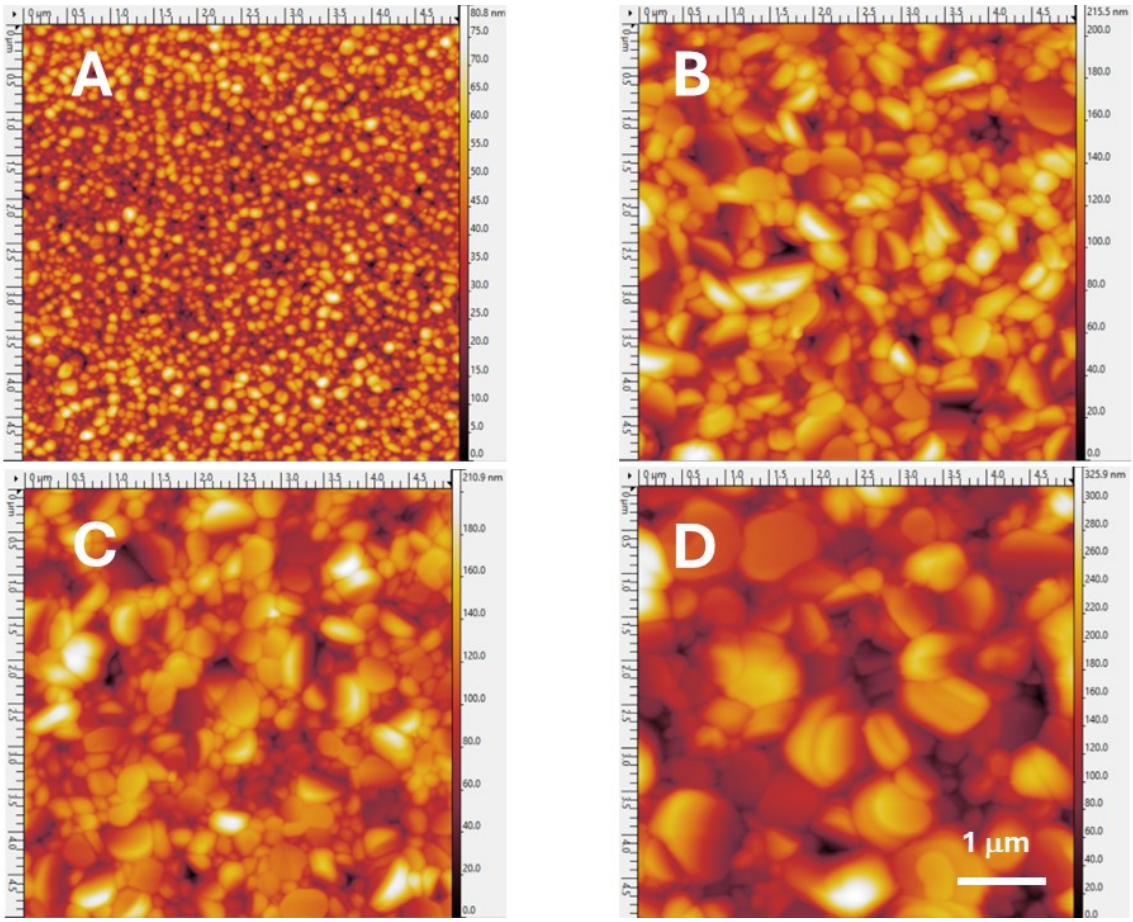

Figure S10. Surface morphology of Sb and Sb-Bi PIM light absorbers employed in the present study. A = CsMAFA-Sb; B = CsMAFA-Sb, 20% DMSO; C = CsMAFA-Sb:Bi, 20% DMSO; D = CsMAFA-Sb:Bi.

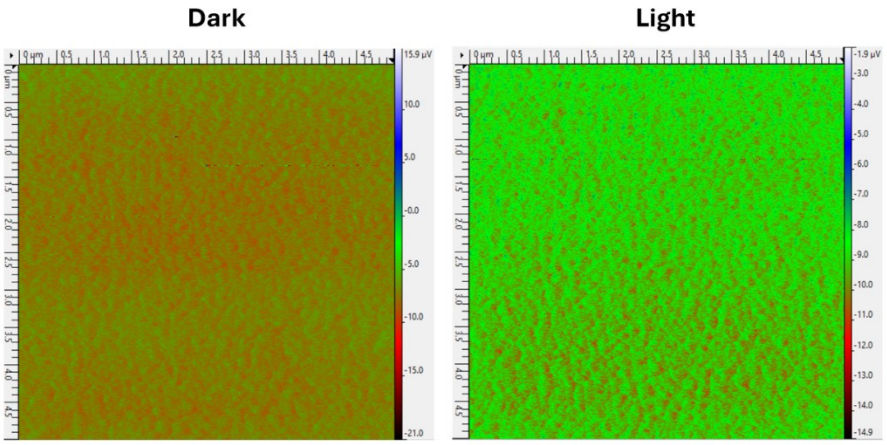

Figure S11. Surface potential measurements of CsMAFA-Sb in dark and under light illumination.

Supplementary note 2: Structural Models and Computational Details

The mixed $A_3(Sb/Bi)_2X_9$ PIM have been built up by $A_3(Sb)_2X_9$ PIM reported in[1] (**Figure S13**). The mixed occupancy of Sb/Bi was simulated via the special quasi-random structure (SQS) approach as implemented in the Alloy Theoretic Automated Toolkit code.[2,3] The SQS is a state-of- the-art method to study solid solutions with two or more components and allowed our models to properly account for the configurational entropy by achieving a mixed occupancy.[4,5]

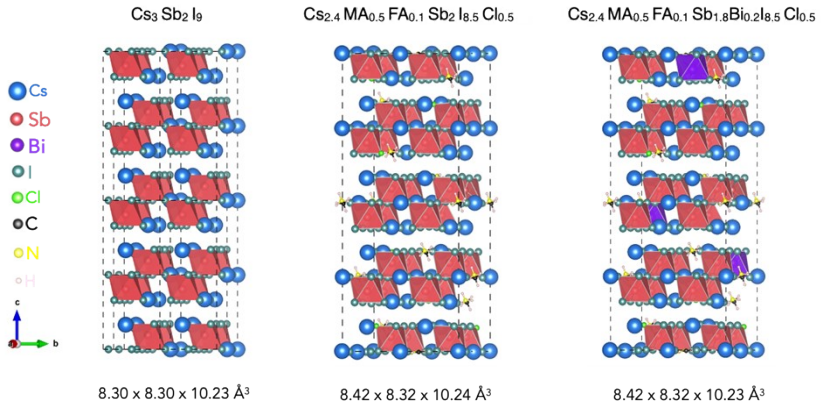

Figure S12. Bulk structure and lattice parameters of the 2D-$A_3(Sb/Bi)_2X_9$ PIMs with A=Cs, FA, MA and X=I, Cl. Color code: Cs (blue), Sb (red), Bi (violet), I (teal), Cl (green), C (black), N (yellow), H (light pink).

On these structures, we performed DFT[6] calculations with periodic boundary conditions (PBC) employing the light–tier1 basis set of numerical atom-centered orbitals (NAO) for each atom,[7] as implemented in the Fritz Haber Institute ab initio molecular simulations (FHI-aims) code.[7–9] Within the FHI-aims framework, the electrons were described by the zero–order regular approximation (atomic ZORA). As self-consistency threshold for electron density convergence, we employed a total energy criterion of 1×10^{-6} eV. We employed the Perdew-Burke-Erzenhof (PBE)[10] exchange correlation functional for all geometry optimizations including the Tkatchenko–Scheffler (TS) correction[11,12] accounting for van der Waals dispersion forces. Our relaxed structures present maximum forces acting on each atom below 0.02 eV/Å. The Γ-centered (2×2×1) k-points sampling mesh have been used; these values ensure converged energies within 3 meV/f.u. Since the PBE functional usually underestimates the band energy gap, we employ the HSE06-TS hybrid functional to calculate the projected density of states (pDOS) and the band energy structures of the PBE-TS optimized geometries.

Additionally, we assessed the average structural distortion for each PIMs structure by evaluating the octahedral distortion factors: the bond length distortion index (D_{oct}) and the bond angle variance (σ^2), calculated according to:

$$D_{oct} = \frac{1}{n}\sum_{i}^{n}\frac{|l_i - l_{av}|}{l_{av}} \qquad \sigma^2 = \frac{1}{m-1}\sum_{i=1}^{n}(\phi_i - \phi_0)^2$$

where l_i and l_{av} are the bond length (B-X) and the average bond length, respectively, in BX_6 octahedra, while m is the number of bond angles (i.e. 12 for octahedra), ϕ_i and ϕ_0 are the bond angle (X-B-X) and the ideal bond angle for a regular octahedron (vertex-core-vertex angles in a perfect octahedron is 90°), respectively.[13,14]

D_{oct} and σ^2 represent the distortion in bond length from the centre of the BX_6 octahedron and the degree of angular distortion from a perfect octahedron, respectively.

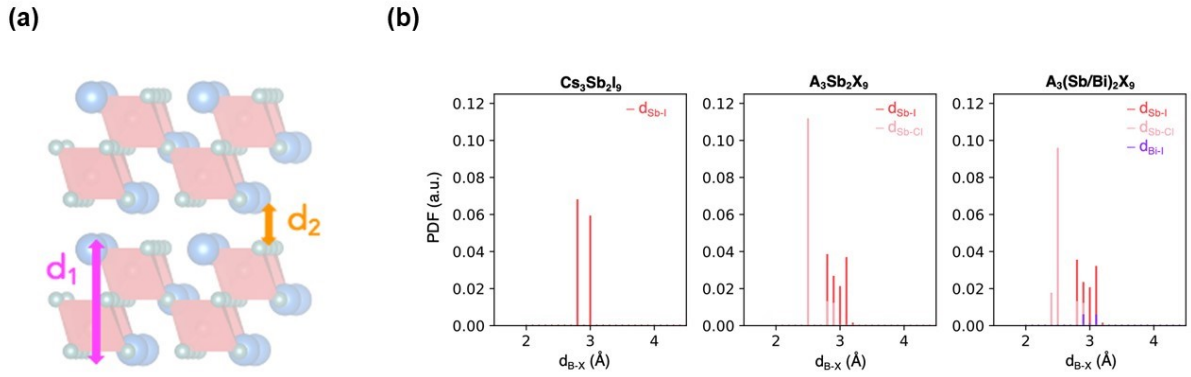

Figure S13. (a) Stacking between layers: d_1 (magenta) and d_2 (orange). (b) Pair distribution function (PDF) analysis of B-X bond lenght (d_{B-X}) in the 2D-$A_3(Sb/Bi)_2X_9$ PIMs with A=Cs, FA, MA and X=I, Cl. From left to right: $Cs_3Sb_2I_9$, $Cs_{2.4}MA_{0.5}FA_{0.1}Sb_2I_{8.5}Cl_{0.5}$ and $Cs_{2.4}MA_{0.5}FA_{0.1}Sb_{1.8}Bi_{0.2}I_{8.5}Cl_{0.5}$. Color code: d_{Sb-I} (red), d_{Sb-Cl} (pink), d_{Bi-I} (violet).

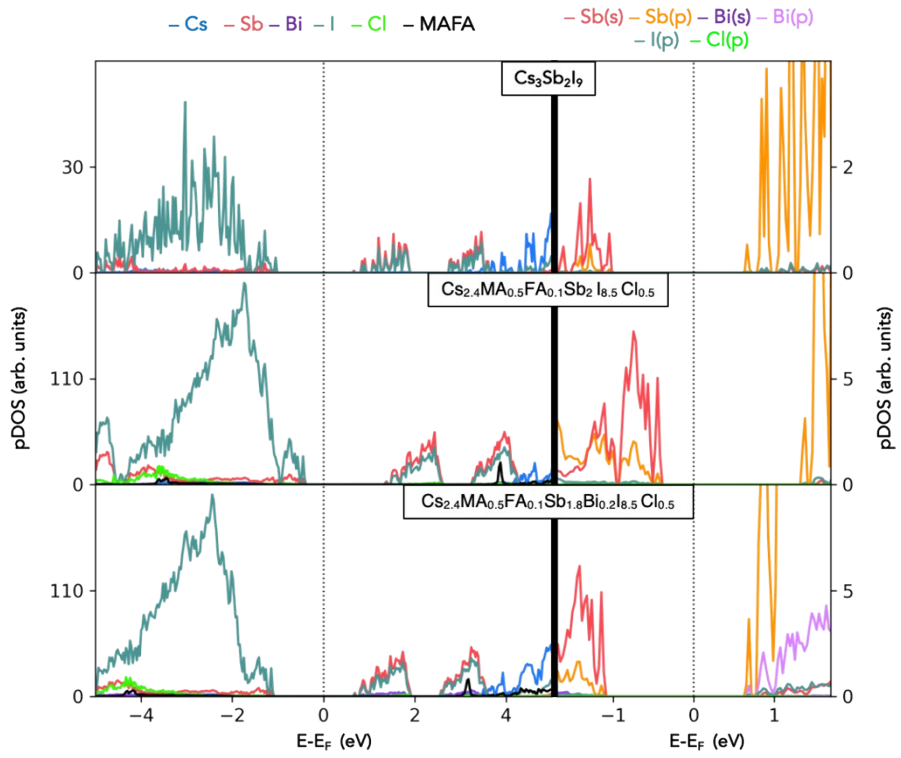

Figure S14. Projected density of states (pDOS) of the 2D-$A_3(Sb/Bi)_2X_9$ PIMs with A=Cs, FA, MA and X=I, Cl. Color code left panel: Cs (blue), Sb (red), Bi (violet), I (teal), Cl (green), MA/FA (black) (on left). Color code right panel: s-states Sb (red), p-states Sb (orange), s-states Bi (violet), p-states Bi (lilac), p-states I (teal), p-states Cl (green). $Cs_{2.4}MA_{0.5}FA_{0.1}Sb_2I_{8.5}Cl_{0.5}$ = CsMAFA-Sb and $Cs_{2.4}MA_{0.5}FA_{0.1}Sb_{1.8}Bi_{0.2}I_{8.5}Cl_{0.5}$ = CsMAFA-Sb:Bi.

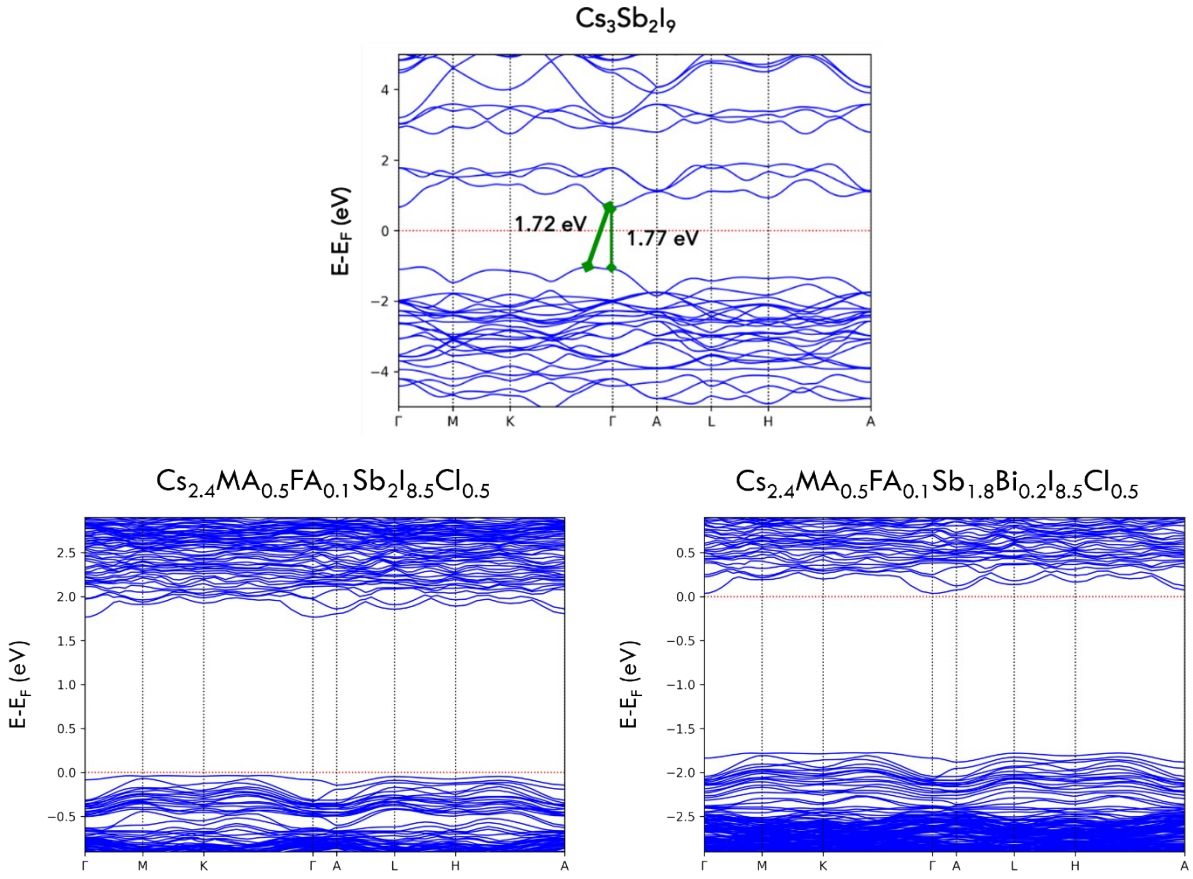

Figure S15. Band energy structure of the 2D-$A_3(Sb/Bi)_2X_9$ PIMs with A=Cs, FA, MA and X=I, Cl. Top panel: $Cs_3Sb_2I_9$, bottom panel left: $Cs_{2.4}MA_{0.5}FA_{0.1}Sb_2I_{8.5}Cl_{0.5}$ (CsMAFA-Sb) and right $Cs_{2.4}MA_{0.5}FA_{0.1}Sb_{1.8}Bi_{0.2}I_{8.5}Cl_{0.5}$ (CsMAFA-Sb:Bi).

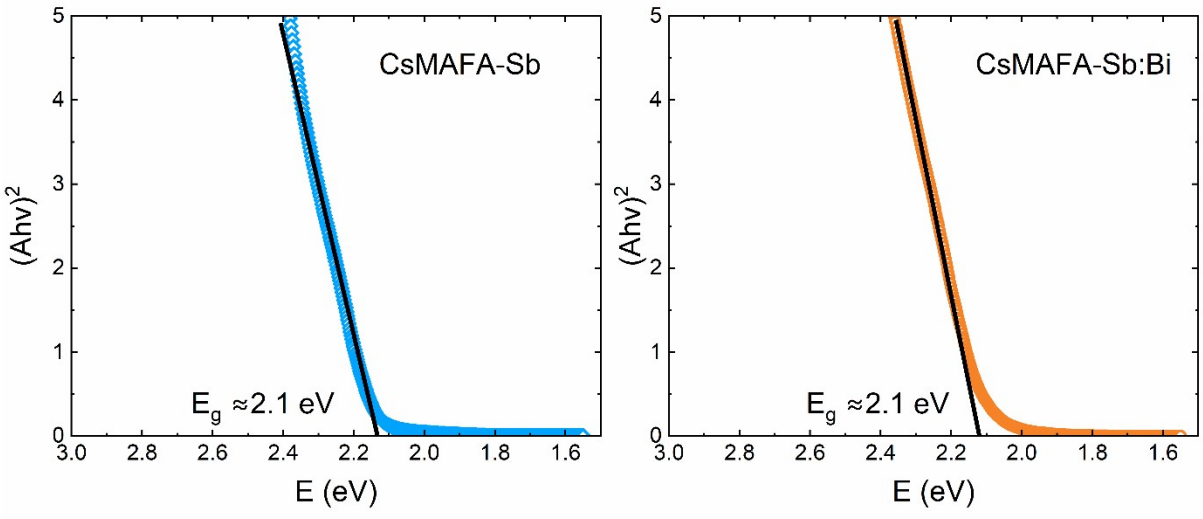

Figure S16. The Tauc plots for CsMAFA-Sb (left panel) and CsMAFA-Sb:Bi films (right panel) for estimating their direct bandgaps.

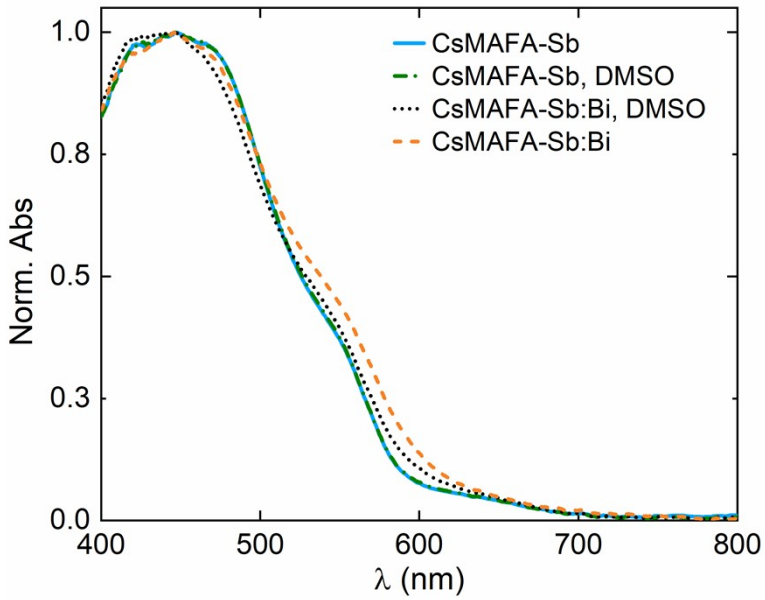

Figure S17. UV-visible absorption spectra of CsMAFA-Sb and CsMAFA-Sb:Bi films processed in DMF and a DMF:DMSO solvent mixture.

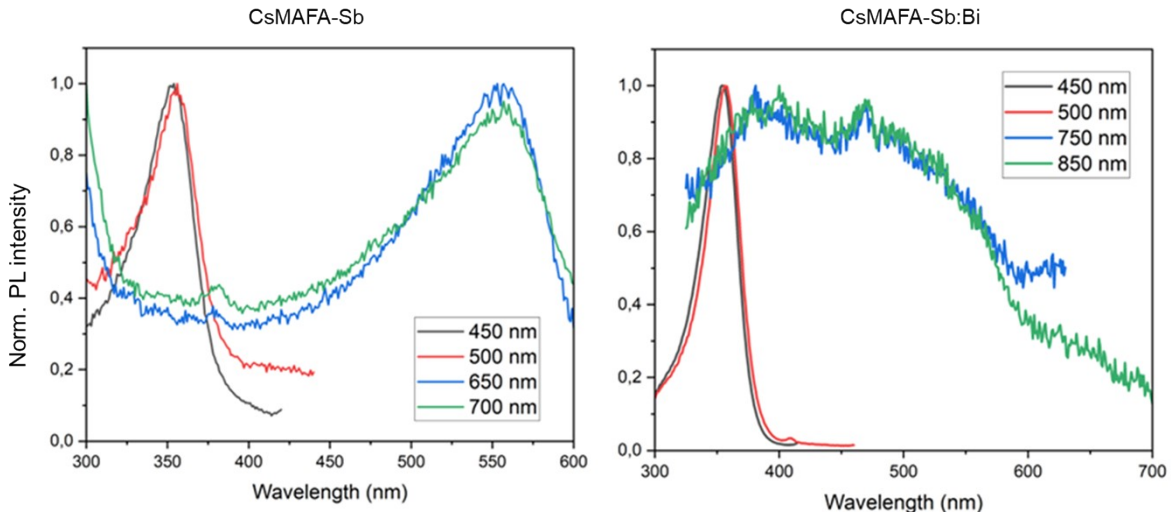

Figure S18. Photoluminescence excitation (PLE) spectra at different emission wavelengths for CsMAFA-Sb and CsMAFA-Sb:Bi.

Supplementary note 3: Calculating charge-carrier mobilities from OPTP transients

To extract the initial charge-carrier mobility from OPTP transients, we use the methodology reported by Wehrenfennig *et al*.[15] and used previously by Righetto et al.[16] for analysis of the charge-carrier dynamics. As discussed by Xia *et al.*,[17] the fractional change in the THz transmission (ΔT/T) can be converted into sheet conductivity (ΔS) using Equation 1:

$$\Delta S = -\epsilon_0 c(n_a + n_b)\left(\frac{\Delta T}{T}\right) \quad (1)$$

where, n_a = 1 and n_b = 2.13 are the refractive indices of vacuum and z-cut quartz substrates respectively, ϵ_0 is the permittivity of free space and c is the speed of light. The sheet conductivity value can be converted to the charge-carrier mobility under the thin-film approximation using equation 2:

$$\mu = \frac{\Delta S A_{eff}}{Ne} \quad (2)$$

where N is the total number photoinduced charge-carriers, A_{eff} is the effective area of overlap between the pump and the THz beam and e denotes the electronic charge. We estimate the number of free charge carriers from the absorbed photon flux (N_p) by using the photon-to-free-carrier branching ratio (φ) where $\varphi = N/N_p$ has a value between 0 and 1. The mathematical expression for the absorbed photon fluence then yields equation 3:

$$N = \varphi N_p = \frac{\varphi E \lambda}{hc}(1 - R - T) \quad (3)$$

Here, E is the total energy delivered by a single excitation pulse of wavelength λ. R and T denote fractional reflection and transmission respectively and are measured experimentally using an FTIR spectrometer. Combining equations 1-3 allows us to extract the effective electron-hole sum mobility from the fractional change in THz transmission:

$$\varphi\mu = -\frac{hc}{E\lambda\,(1 - R - T)}\left(\frac{\Delta T(\omega)}{T(\omega)}\right) A_{eff}\epsilon_0 c(n_a + n_b) \quad (4)$$

The effective mobility value extracted using the above regimen corresponds to the sum of the mobility of electrons and holes immediately after photoexcitation.

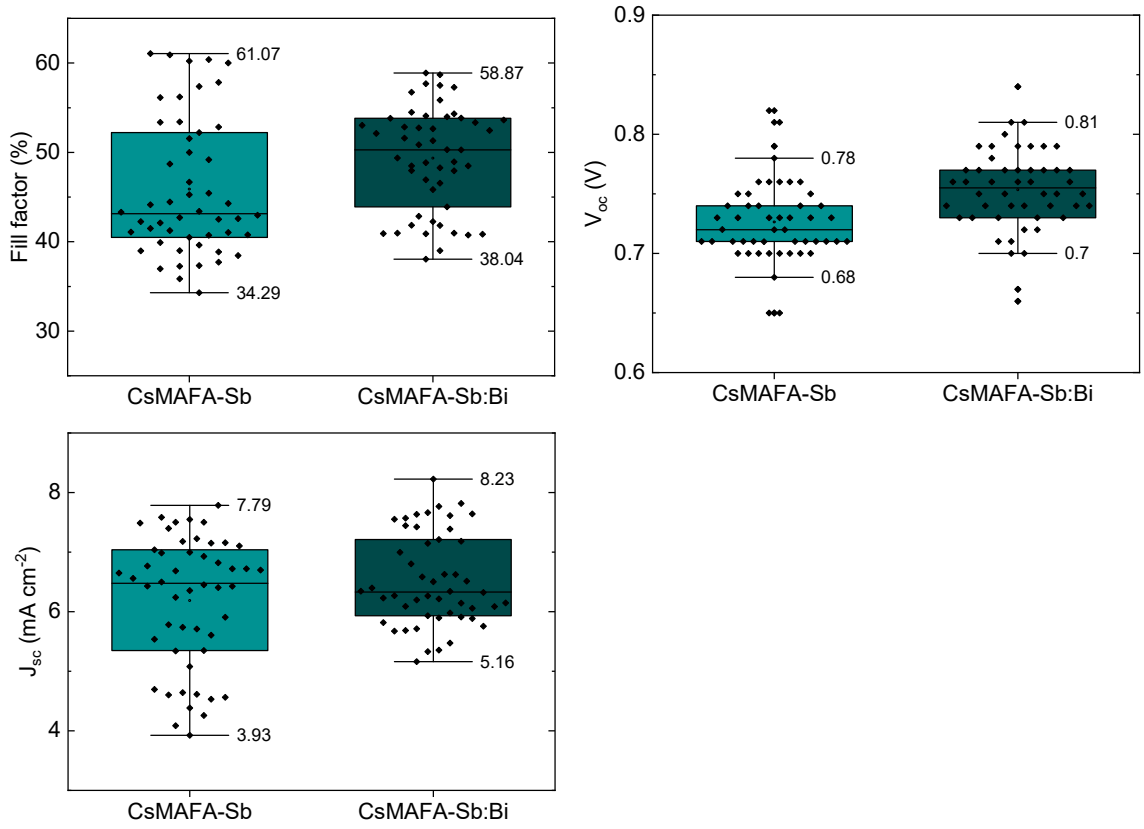

Figure S19. Statistical distribution of photovoltaic parameters (fill factor, short circuit current, and open circuit current) over 50 devices.

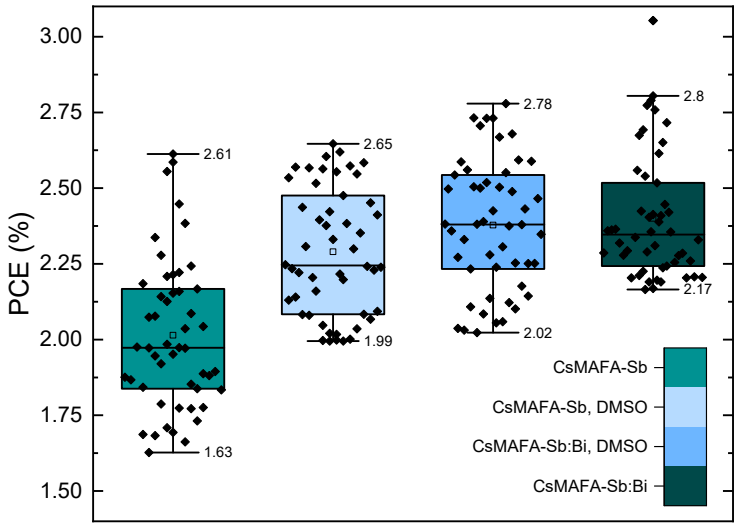

Figure S20. The statistical distributions of power conversion efficiency over 50 devices of CsMAFA-Sb; CsMAFA-Sb, DMSO; CsMAFA-Sb:Bi, DMSO; and CsMAFA-Sb:Bi.

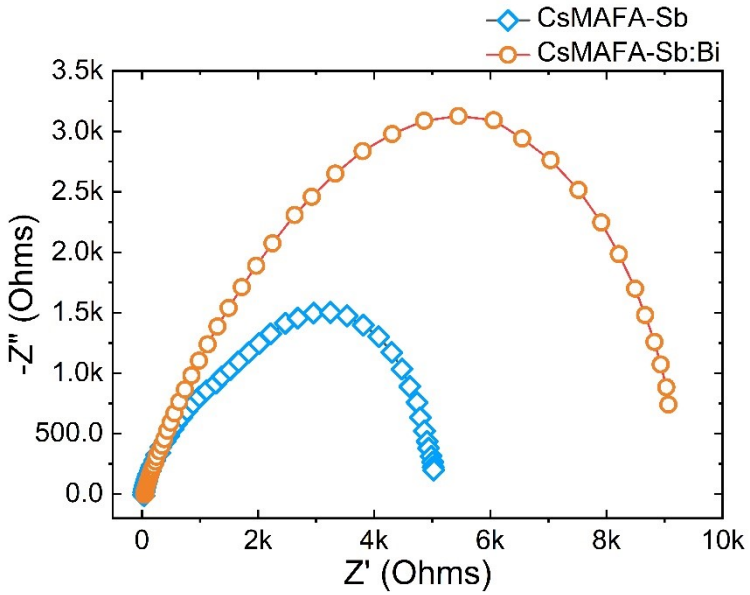

Figure S21. Nyquist plots, obtained from EIS measurements of CsMAFA-Sb and CsMAFA-Sb:Bi devices.

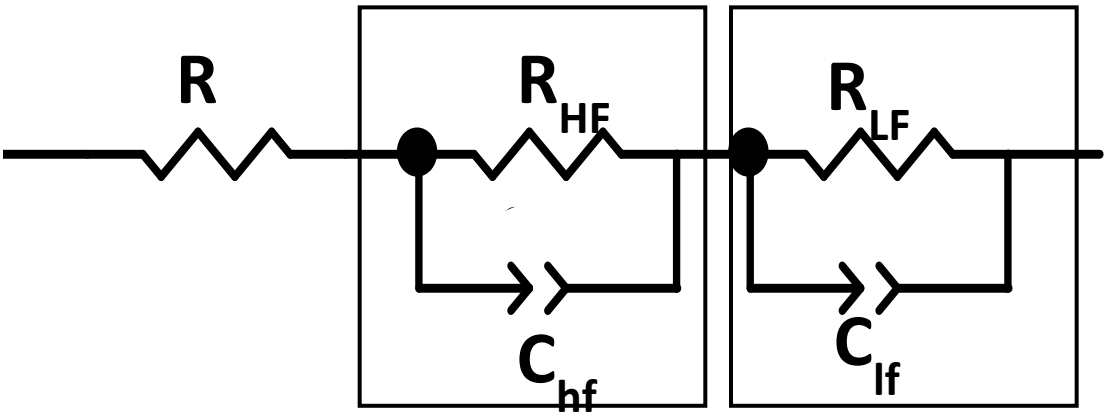

Figure S22. Equivalent Electrical Circuit for fitting the impedance data. Here, two Randle circuits denoted by R_{HF}/C_{HF} and R_{LF}/C_{LF}, are related to high- and low frequency processes.

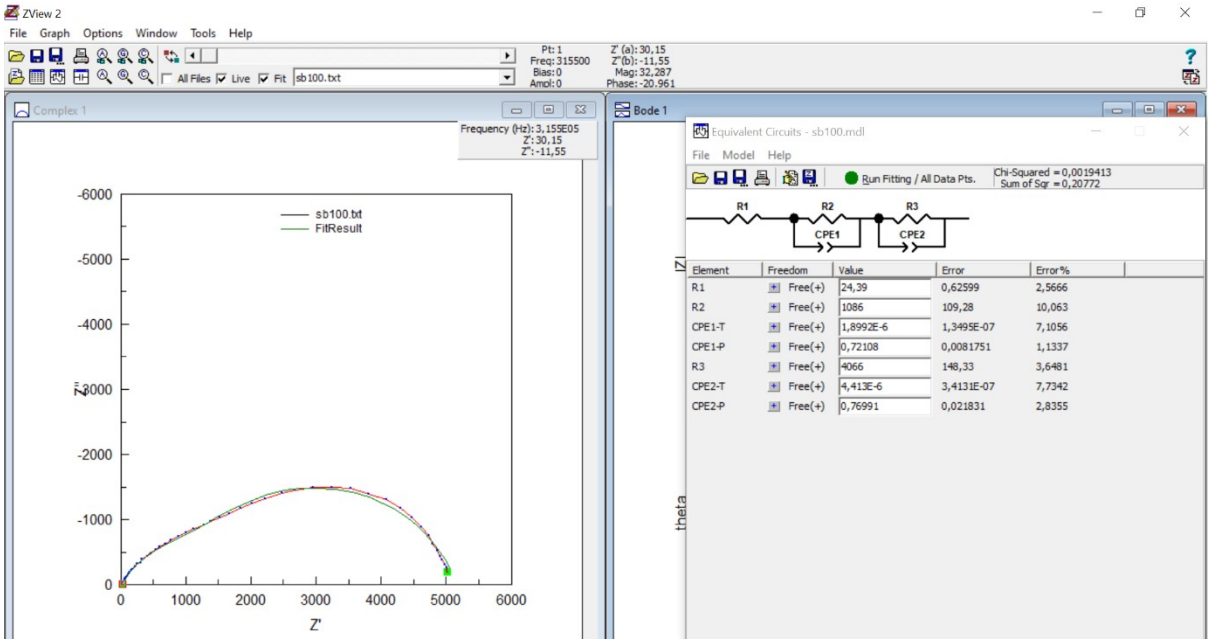

Figure S23. Z-view software panel displays the fitting of Nyquist plot with the appropriate electrical equivalent circuit.

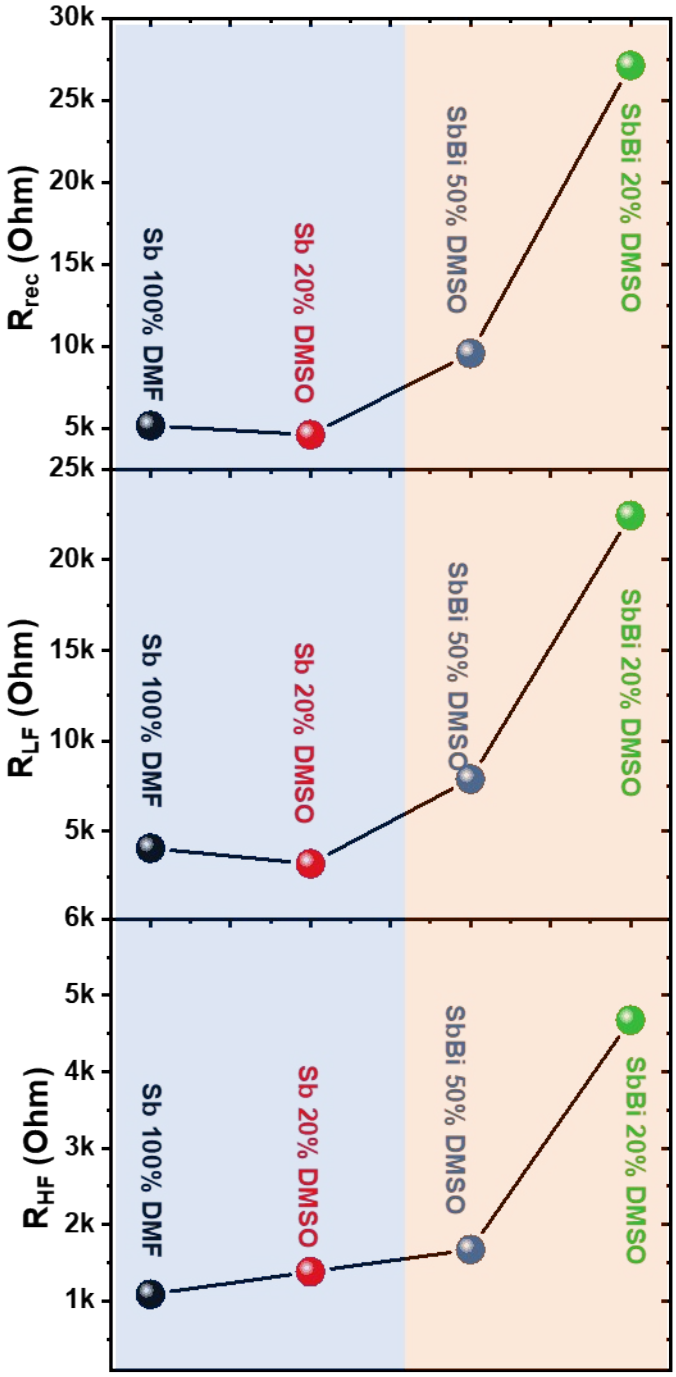

Figure S24. Fitted high frequency-, low frequency- and total recombination resistance parameters for CsMAFA-Sb and CsMAFA-Sb:Bi PIM based solar cells.

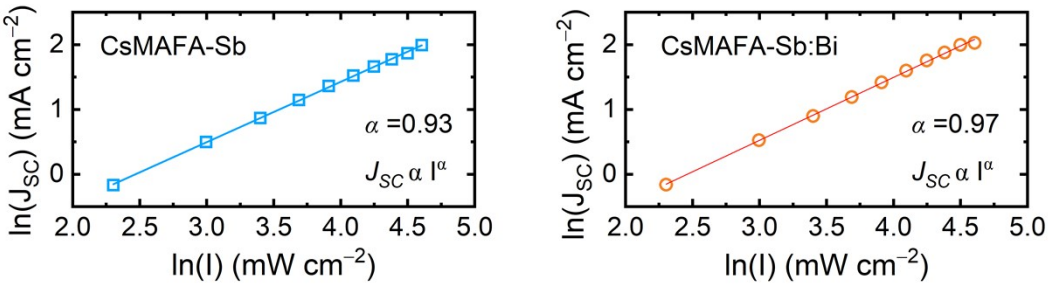

Figure S25. log-log plots of J_{SC} versus light intensity for CsMAFA-Sb and CsMAFA-Sb:Bi devices.

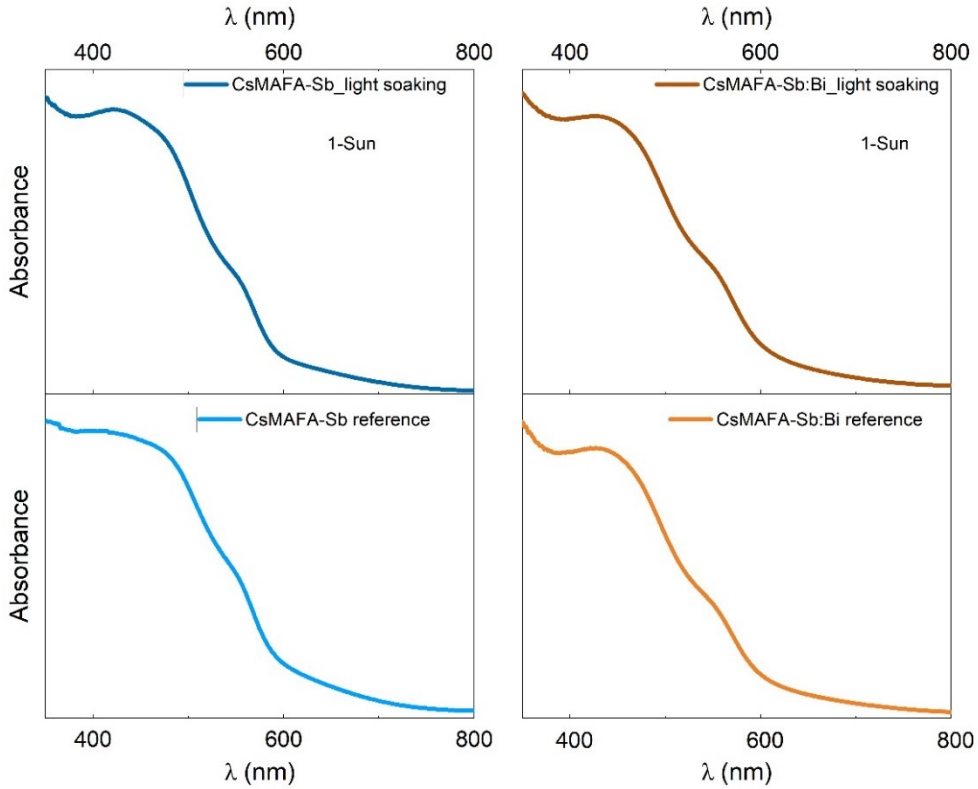

Figure S26. Absorption spectra of the CsMAFA-Sb and CsMAFA-Sb:Bi films on glass before and after light-soaking under 1-Sun for over 100 hours under N_2 atmosphere.

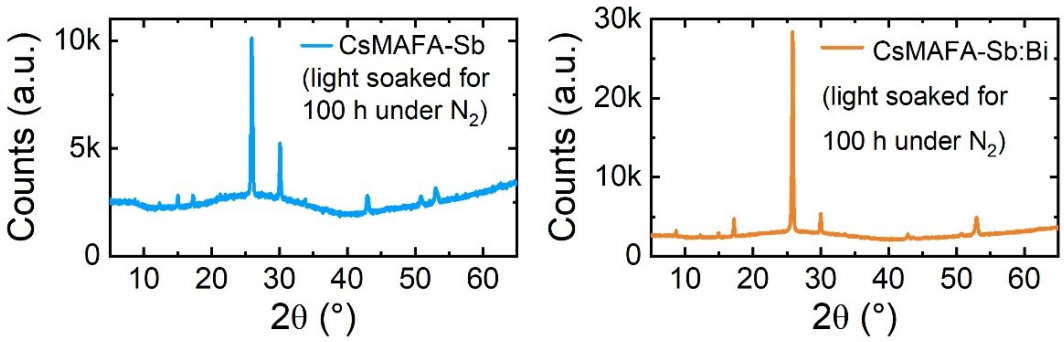

Figure S27. XRD patterns of the CsMAFA-Sb and CsMAFA-Sb:Bi films after light-soaking under 1-Sun for over 100 hours under N_2 atmosphere.

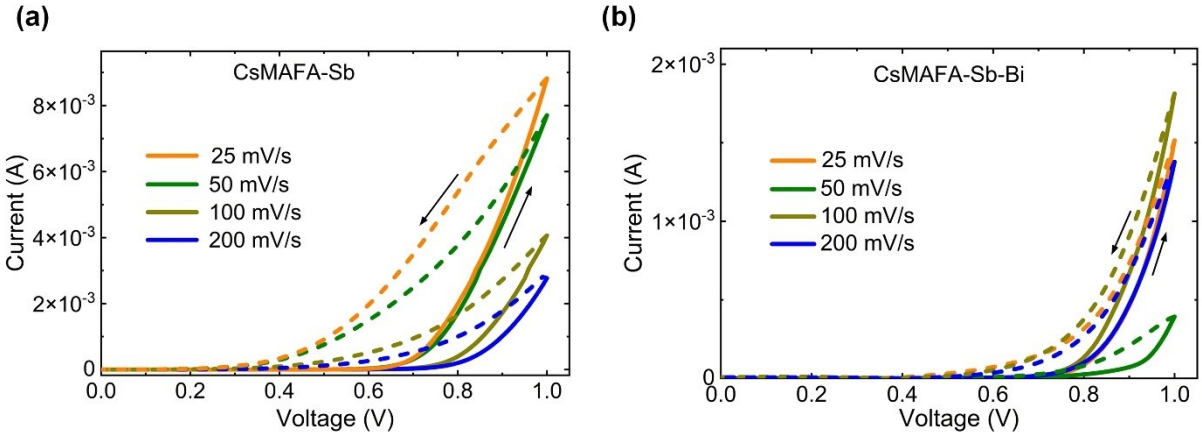

Figure S28. *J-V* curves at different scan rates of (a) CsMAFA-Sb and (b) CsMAFA-Sb:Bi.

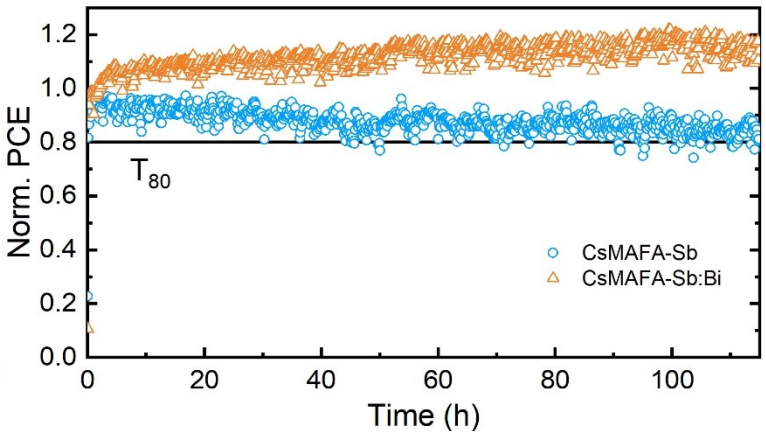

Figure S29. Maximum power point (MPP) tracking of unencapsulated CsMAFA-Sb and CsMAFA-Sb:Bi devices under N_2 environment under 0.1-Sun illumination at room temperature.

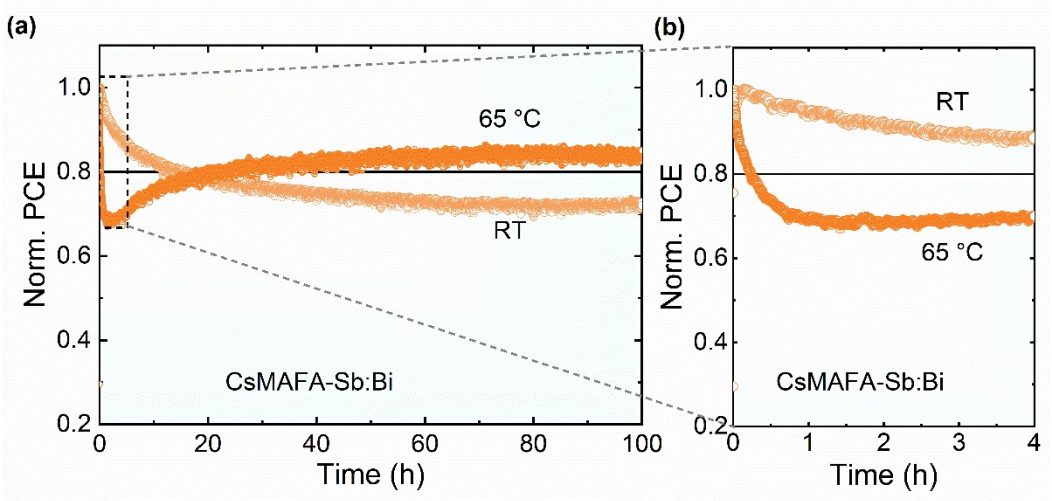

Figure S30. (a) Comparison of MPP trends over time for CsMAFA-Sb:Bi at room temperature, ~27°C, (2.5% initial PCE) and 65°C (2.3% initial PCE) and (b) the corresponding initial period of up to 4 h.

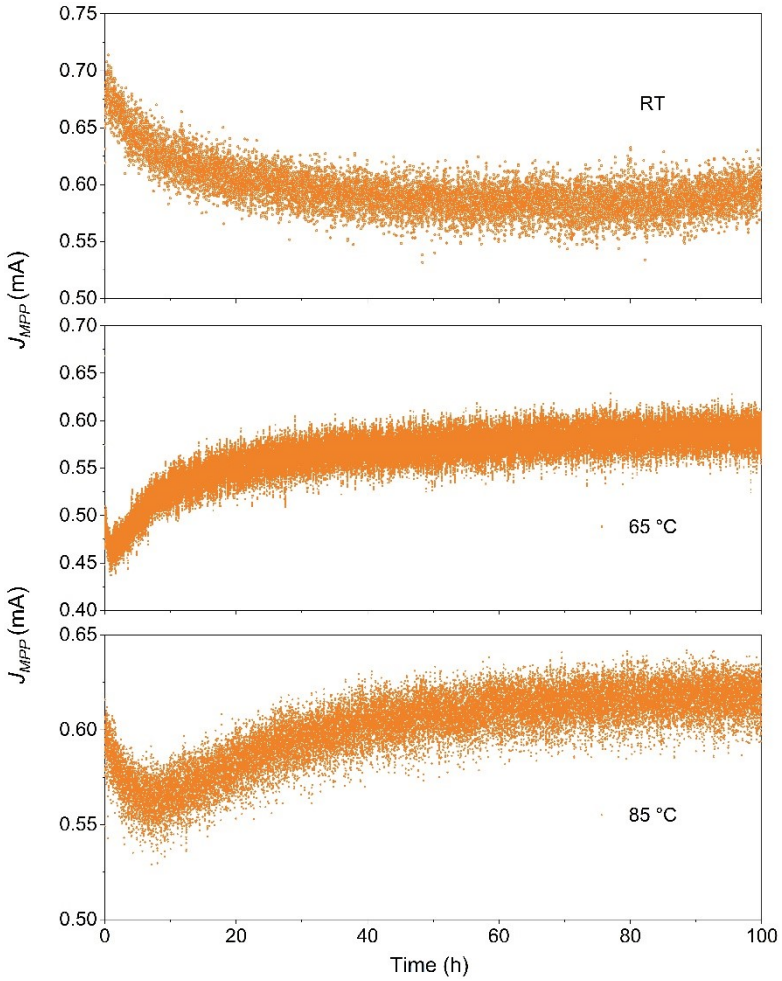

Figure S31. The J_{MPP} trends corresponding to the MPP tracking data shown in **Figures 7** and **S30**.

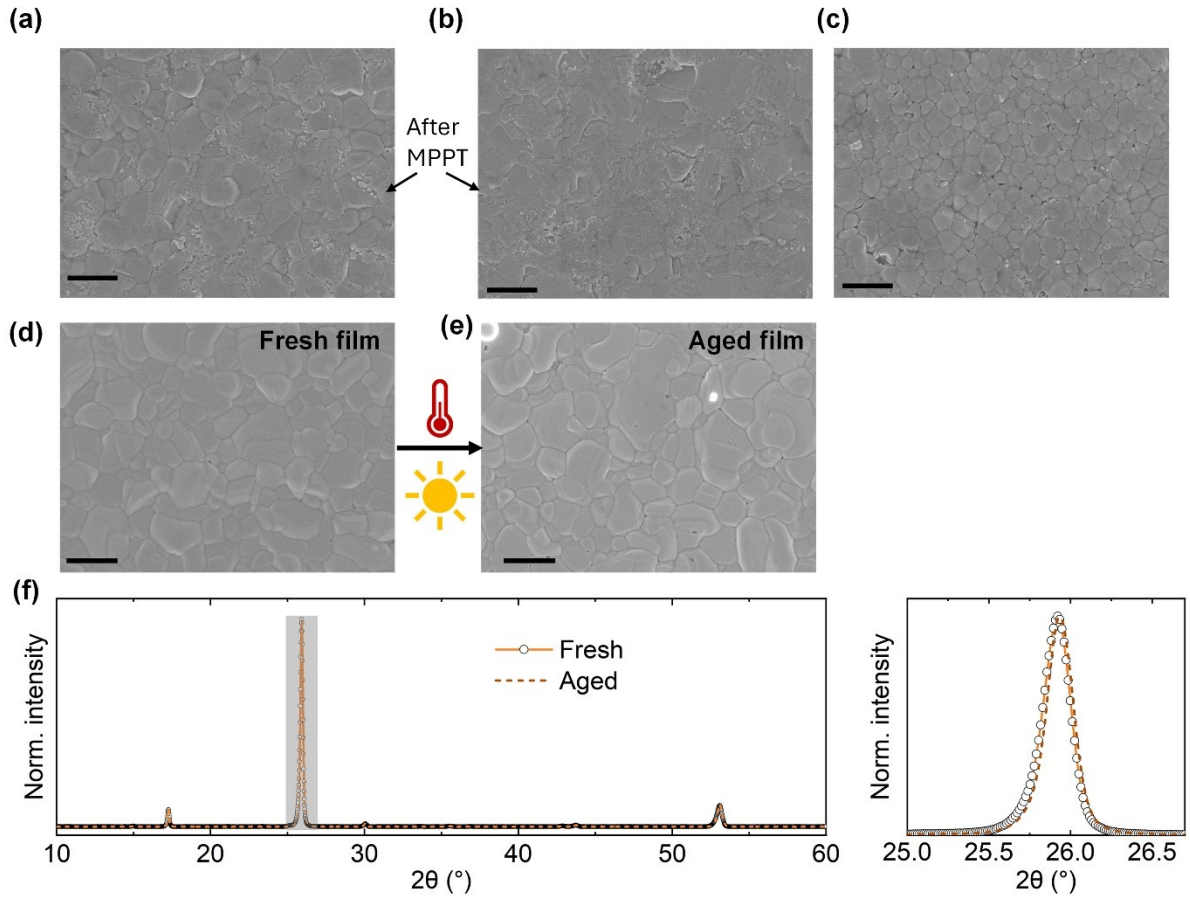

Figure S32. Aged devices and films of CsMAFA-Sb:Bi under N_2 environment.
(a) and (b) Representative top-view SEM images of the CsMAFA-Sb:Bi layer in aged devices after MPP tracking at 85°C. We wiped both the Au electrode and P3HT layers and collected the SEM images. (c) Top-view SEM image of the CsMAFA-Sb:Bi layer in the non-electrode portion of the aged device after MPPT at 85°C. The scale bars in all the SEM images are 1 micron. (d) and (e) SEM images and (f) XRD patterns of a CsMAFA-Sb:Bi film on FTO/c-TiO_2 before and after annealing at 85°C for more than 24 hours under constant illumination (approximately 0.5-Sun).

Supplementary note 4

The grain fusing (**Figures S32a,b**) didn't happen in the areas of device where there is no electrode present (**Figures S32c**) but still exposed to the same amount of light and heat, which, in turn, suggests that the electric bias is also necessary in the grain fusing process. To further supports this observation, we aged just the CsMAFA-Sb:Bi film atop c-TiO_2 layer (*i.e.,* half device) more than 24 hours (**Figures S32d and S32e**). The SEM images of the fresh and aged films more of less look similar, except a few fused grains in **Figure S32e**. We didn't observe any noticeable changes to the XRD pattern (**Figure S32f**), suggesting the crystal structure remained intact after the thermal stress.

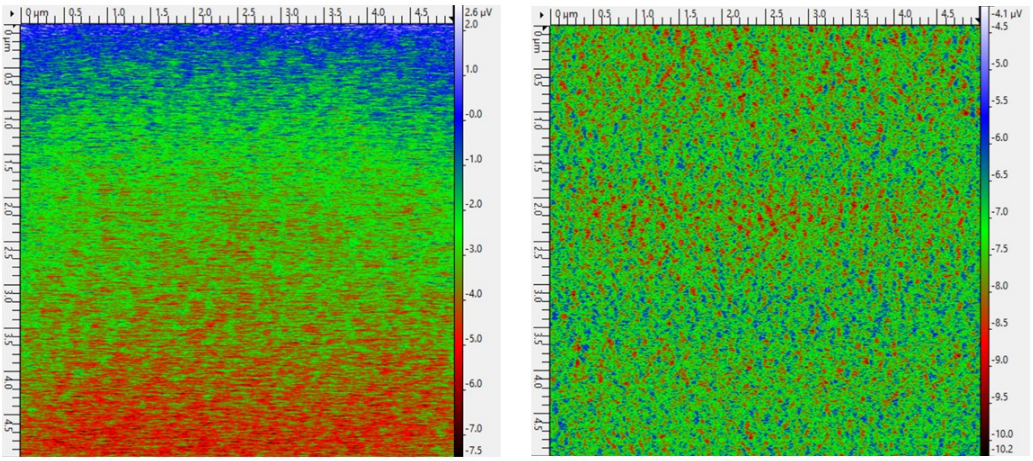

Figure S33. Illustration of KPFM surface potential mapping for CsMAFA-Sb on FTO without (left-hand panel) and with a c-TiO_2 layer (right-hand panel).

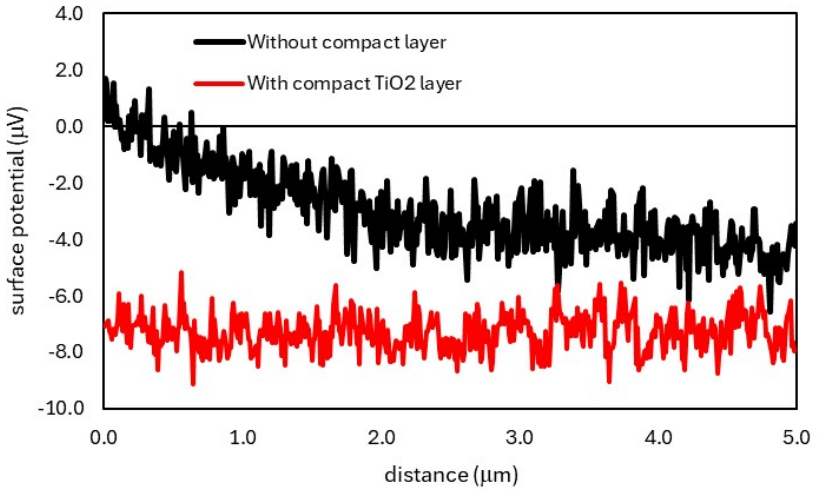

Figure S34. Illustration of surface charging on the surface of CsMAFA-Sb under KPFM imaging with and without a c-TiO_2 layer. Note the scan direction is from left to right.

Table S1. Rietveld refinement parameters of CsMAFA-Sb and CsMAFA-Sb: Bi thin film samples obtained from the powder X-ray diffraction data at room temperature. The numbers in parentheses are the estimated standard deviations of the last significant figure.

Parameter	CsMAFA-Sb	CsMAFA-Sb:Bi
Space group	*P*-3*m1*	*P*-3*m1*
a = b (Å)	8.43(7)	8.75(9)
c (Å)	10.38(3)	10.46(5)
V (Å^3)	638.91(5)	642.78(7)
R_{wp} (%)	4.73	4.98
R_{exp} (%)	1.83	1.74
c^2	2.4	1.8

Table S2. Atomic positions of CsMAFA-Sb and CsMAFA-Sb:Bi thin film samples obtained from the powder X-ray diffraction data at room temperature. The numbers in parentheses are the estimated standard deviations of the last significant figure.

CsMAFA-Sb

Atom	Wyckoff position	*x*	*y*	*z*	*g*	100xU_{iso}(Å)^2
Cs1	1*a*	0	0	0	1.00	0.06(3)
Cs2	2*d*	0.33	0.67	0.67	1.00	0.04(12)
Sb	2*d*	0.33(3)	0.67(3)	0.19(3)	0.90	0.07(2)
I1	*3e*	0.50	0	0	1.00	0.17 (5)
I2	*6i*	0.1670(2)	0.832(5)	0.339(7)	0.945	0.29(9)
Cl2	*6i*	0.1670(2)	0.832(5)	0.339(7)	0.055	0.29(7)

CsMAFA-Sb:Bi

Atom	Wyckoff position	*x*	*y*	*z*	*g*	100xU_{iso}(Å)^2
Cs1	1*a*	0	0	0	1.00	0.06(3)
Cs2	2*d*	0.33	0.67	0.67	1.00	0.04(12)
Sb	2*d*	0.33(3)	0.67(3)	0.19(3)	0.90	0.07(2)
Bi	*2d*	0.33(3)	0.67(3)	0.19(3)	0.10	0.07(2)
I1	*3e*	0.50	0	0	1.00	0.17(5)
I2	6*i*	0.1670(2)	0.832(5)	0.1670(7)	0.945	0.25(2)
Cl2	6*i*	0.1670(2)	0.832(5)	0.1670(7)	0.055	0.25 (2)

Table S3. Surface atomic ratios of CsMAFA-Sb and CsMAFA-Sb:Bi films from XPS data analysis.

Material	Element	Atomic ratio
CsMAFA-Sb	Cs	2
	Sb	2
	I	4.7
	Cl	0.7
CsMAFA-Sb:Bi	Cs	4
	Sb	2
	Bi	0.3
	I	10.6
	Cl	0.6

Table S4. Mean grain size extracted by watershed marking of the AFM images shown in **Figure S7**.

Material	Mean Grain Size (nm)
A CsMAFA-Sb 100% DMF	100
B CsMAFA-Sb 20% DMSO 80% DMF	170
C CsMAFA-Sb/Bi 90/10 in 20% DMSO 80% DMF	140
D CsMAFA-Sb/Bi 90/10 in 50% DMSO 50% DMF	270

Table S5. Surface roughness calculations for the studied perovskite-inspired absorbers for the whole area of an AFM image (5x5 mm^2).

Material	Root mean square roughness (nm)
CsMAFA-Sb	**2.05**
CsMAFA-Sb, 20% DMSO	**1.99**
CsMAFA-Sb:Bi, 20% DMSO	**1.91**
CsMAFA-Sb:Bi	**3.30**

Table S6. Average surface potential recorded across the centre of the PIM samples (refer to **Figure 2** in the main manuscript).

Surface potential profile across middle of sample	**CsMAFA-Sb (mV)**	**CsMAFA-Sb:Bi (mV)**
Dark	-7	-6.5
Light	-9	-9.5

Table S7. Lattice parameters, stacking between layers (d_1 and d_2 in Figure S14) at the PBE-TS level of theory and bandgap (indirect/direct) at HSE06-TS level of theory of 2D-$A_3(Sb/Bi)_2X_9$ PIMs relaxed structures.

2D-$A_3Sb_2X_9$	Lattice parameters/f.u.	Stacking (Å)	Octahedral distortion	BandGap (eV)

	(Å)								
	a	b	c	d_1	d_2	$\%D_{oct}$	σ^2	Indirect	Direct
$Cs_3Sb_2I_9$	8.30	8.30	10.23	6.95	3.28	3%	14.4	1.72	1.77
$Cs_{2.4}MA_{0.5}FA_{0.1}Sb_2I_{8.5}Cl_{0.5}$ (CsMAFA-Sb)	8.42	8.32	10.24	6.94	3.29	4%	17.6	1.81	1.85
$Cs_{2.4}MA_{0.}FA_{0.1}Sb_{1.8}Bi_{0.2}I_{8.5}Cl_{0.5}$ (CsMAFA-Sb:Bi)	8.42	8.32	10.23	6.95	3.29	4%	18.2	1.82	1.87

Table S8. Photovoltaic parameters of CsMAFA-Sb and CsMAFA-Sb:Bi devices before and after maximum power point tracking under 1-Sun illumination, measured under 1-Sun.

Device	Scan direction	PCE (%)	FF (%)	J_{SC} (mA cm^{-2})	V_{OC} (V)	Hysteresis (%)
CsMAFA-Sb	REV (before)	2.2	46.08	5.85	0.79	11.42
	FOR (before)	1.89	44.40	5.42	0.79	
	REV (after)	0.94	30.22	4.80	0.65	15.90
	FOR (after)	0.79	27.95	4.41	0.64	
CsMAFA-Sb:Bi	REV (before)	2.3	39.55	7.8	0.72	3.1
	FOR (before)	2.15	40.31	7.4	0.72	
	REV (after)	1.78	50.55	4.9	0.71	14
	FOR (after)	1.53	48.86	4.7	0.66	

Table S9. Distortion angles and bond lengths of the pnictogen halide octahedra, extracted from Rietveld refined structures of CsMAFA-Sb and CsMAFA-Sb:Bi.

Sample	Distortion angle (°)	Bond length of Sb-I in Å	Bond distance between Sb-Sb in Å	Distortion index (%)
CsMAFA-Sb	173.48	3.0	8.06	4.4
CsMAFA-Sb:Bi	169.85	3.18	8.46	6.3

Table S10. Relevant recent operational stability studies of comparable organic-inorganic hybrid lead halide perovskite solar cells (*n-i-p* structure) using P3HT (no dopants) and polymeric hole-transport materials.

Device structure	Measurement conditions	Residual PCE details	Ref.
FTO/c-TiO_2/m-TiO_2+perovskite/P3HT/ Au	Maximum power point tracking of encapsulated device under AM 1.5 G (1-Sun) illumination at room temperature	20% of the initial PCE after 100 hours	[18]
FTO/ZTO/m-TiO_2/perovskite/P3HT/ Au	Maximum power point tracking of encapsulated device under AM 1.5 G (1-Sun) illumination at 85 °C	T_{80} of approximately 40 hours	[19]
FTO/c-TiO_2/m-TiO_2/PEAI/ perovskite /PEAI/polymeric HTL/Au	Maximum power point tracking under AM 1.5 G (1-Sun) illumination at 65 °C under continuous N_2 flow	T_{80} of < 100 hours (no dopants) T_{80} of 200 hours (with dopants)	[20]

ZTO = $ZnTiO_3$ electron transporting layer with ZnS surface

Table S11. Photovoltaic parameters of the CsMAFA-Sb:Bi devices before and after maximum power point tracking under 1-Sun illumination and at 85 °C, measured under 1-Sun.

	Scan direction	PCE (%)	FF (%)	J_{SC} (mA cm^{-2})	V_{OC} (V)	Hysteresis (%)
CsMAFA-Sb:Bi	REV (before)	2.46	38.7	9.3	0.685	23
	FOR (before)	1.88	35.6	8.3	0.638	
	REV (after)	2.43	37.5	9.1	0.710	4
	FOR (after)	2.35	36.4	9.1	0.705	

References

[1] N. Lamminen, G. K. Grandhi, F. Fasulo, A. Hiltunen, H. Pasanen, M. Liu, B. Al-Anesi, A. Efimov, H. Ali-Löytty, K. Lahtonen, P. Mäkinen, A. Matuhina, A. B. Muñoz-García, M. Pavone, P. Vivo, *Adv. Energy Mater.* **2023**, *13*, 2203175.

[2] A. van de Walle, M. Asta, G. Ceder, *Calphad* **2002**, *26*, 539.

[3] A. van de Walle, R. Sun, Q.-J. Hong, S. Kadkhodaei, *Calphad* **2017**, *58*, 70.

[4] A. Massaro, A. B. Muñoz-García, P. P. Prosini, C. Gerbaldi, M. Pavone, *ACS Energy Lett.* **2021**, *6*, 2470.

[5] A. Massaro, A. Langella, A. B. Muñoz-García, M. Pavone, *J. Am. Ceram. Soc.* **2023**, *106*, 109.

[6] K. Burke, *J. Chem. Phys.* **2012**, *136*, 150901.

[7] V. Blum, R. Gehrke, F. Hanke, P. Havu, V. Havu, X. Ren, K. Reuter, M. Scheffler, *Comput. Phys. Commun.* **2009**, *180*, 2175.

[8] V. Havu, V. Blum, P. Havu, M. Scheffler, *J. Comput. Phys.* **2009**, *228*, 8367.

[9] E. van Lenthe, J. G. Snijders, E. J. Baerends, *J. Chem. Phys.* **1996**, *105*, 6505.

[10] J. P. Perdew, K. Burke, M. Ernzerhof, *Phys. Rev. Lett.* **1996**, *77*, 3865.

[11] A. Tkatchenko, M. Scheffler, *Phys. Rev. Lett.* **2009**, *102*, 073005.

[12] A. Tkatchenko, R. A. DiStasio, R. Car, M. Scheffler, *Phys. Rev. Lett.* **2012**, *108*, 236402.

[13] J. H. Van Vleck, *J. Chem. Phys.* **1939**, *7*, 72.

[14] W. H. Baur, *Acta Crystallogr. B* **1974**, *30*, 1195.

[15] C. Wehrenfennig, G. E. Eperon, M. B. Johnston, H. J. Snaith, L. M. Herz, *Adv. Mater.* **2014**, *26*, 1584.

[16] M. Righetto, Y. Wang, K. A. Elmestekawy, C. Q. Xia, M. B. Johnston, G. Konstantatos, L. M. Herz, *Adv. Mater.* **2023**, *35*, 2305009.

[17] C. Q. Xia, J. Peng, S. Poncé, J. B. Patel, A. D. Wright, T. W. Crothers, M. Uller Rothmann, J. Borchert, R. L. Milot, H. Kraus, Q. Lin, F. Giustino, L. M. Herz, M. B. Johnston, *J. Phys. Chem. Lett.* **2021**, *12*, 3607.

[18] E. H. Jung, N. J. Jeon, E. Y. Park, C. S. Moon, T. J. Shin, T.-Y. Yang, J. H. Noh, J. Seo, *Nature* **2019**, *567*, 511.

[19] F. Cao, F. Cheng, X. Huang, X. Dai, Z. Tang, S. Nie, J. Yin, J. Li, N. Zheng, B. Wu, *Adv. Funct. Mater.* **2022**, *32*, 2201423.

[20] S. Kim, S. Sabury, C. A. R. Perini, T. Hossain, A. O. Yusuf, X. Xiao, R. Li, K. R. Graham, J. R. Reynolds, J.-P. Correa-Baena, *ACS Energy Lett.* **2024**, *9*, 4501.